Catalysis Today 175 (2011) 450–459

Contents lists available at ScienceDirect

Catalysis Today

journal homepage: www.elsevier.com/locate/cattod

Fischer–Tropsch synthesis: Effect of promoter type on alumina-supported Mo carbide catalysts

Dai-Viet N. Vo[a], Tuan-Huy Nguyen[a], Eric M. Kennedy[b], Bogdan Z. Dlugogorski[b], Adesoji A. Adesina[a,*]

[a] Reactor Engineering & Technology Group, School of Chemical Engineering, The University of New South Wales, Sydney, NSW 2052, Australia
[b] Priority Research Centre for Energy, University of Newcastle, Callaghan, NSW 2308, Australia

ARTICLE INFO

Article history:
Received 31 October 2010
Received in revised form 4 February 2011
Accepted 23 April 2011
Available online 1 June 2011

Keywords:
Fischer–Tropsch synthesis
Promoted-molybdenum carbide
Temperature-programmed carburization

ABSTRACT

Molybdenum carbide catalysts promoted with K, Na, Co, and Ce have been synthesized by temperature-programmed carburization using a mixture of H_2/C_3H_8 and evaluated for the Fischer–Tropsch synthesis. Both α- and β-Mo carbide catalysts were produced during carburization via the formation of oxy-carbide intermediate phase. The two-stage Mo carbide synthesis appeared to be characterized by a compensation effect and isokinetic relationship for both promoted and undoped catalysts suggesting that the solid state transformation mechanism was similar across the promoters. The catalysts possessed relatively high BET area (177–210 $m^2\,g_{cat}^{-1}$) with finely dispersed Mo carbide particles (ca. 10 nm) on the alumina support. The presence of weak and strong acid–base sites was also confirmed by NH_3 and CO_2-TPD runs. CO hydrogenation rate increased with H_2 composition reaching optimal activity at y_{H_2} between 0.67 and 0.75. FT activity improved with promoter addition in the order; $K–MoC_{1-x}/Al_2O_3 > Na–MoC_{1-x}/Al_2O_3 > Ce–MoC_{1-x}/Al_2O_3 > Co–MoC_{1-x}/Al_2O_3 > MoC_{1-x}/Al_2O_3$ while chain growth probability varied with feed composition and was enhanced by all promoters. The reaction rate data were adequately described by an Eley–Rideal model.

1. Introduction

The depletion of petroleum resources and environmental concerns have motivated interest in advanced technologies for clean fuels production. Fischer–Tropsch synthesis (FTS) is considered one of the most promising alternatives for non-oil based GTL fuels processes. Traditional FT catalysts suffer from deactivation due to carbon deposition but Mo carbide is tolerant of carbon deposition and has Pt-like catalytic properties [1]. It has been used for different catalytic reactions, namely NH_3 synthesis [2], NO reduction [3], hydrotreating [4], and dry reforming [5]. Thus, a Mo carbide catalyst system has been investigated in this work for hydrocarbon synthesis. MoC_{1-x} ($0 \le x < 1$) is typically produced via temperature-programmed carburization with H_2/light alkane mixture [6]. However, it has been found that utilization of higher hydrocarbon as carbon source reduced carburization temperature and hence improved catalyst surface area [7]. While there is strong evidence for the effect of alkali promoters on conventional FT catalysts, comparative data are unavailable on the promising Mo carbide catalyst. Therefore, the objective of this paper was to study the effect of different types of metal promoters (alkali, transition and rare-earth) on the physicochemical properties and FT performance of the Mo carbide catalyst.

2. Experimental

γ-Al_2O_3 support pretreated at 973 K in air for 6 h to ensure thermal stability was co-impregnated with calculated amounts of $(NH_4)_6Mo_7O_{24}{\cdot}4H_2O$ and the corresponding promoter precursor – K_2CO_3, Na_2CO_3, $Ce(NO_3)_3$, $Co(NO_3)_2$ in aqueous solution. The impregnated slurry was dried in an oven for 16 h at 403 K and subsequently calcined in air at 773 K for 5 h. The resulting solid was carburized with a mixture of H_2:C_3H_8 = 5:1 at 973 K and 10 K min^{-1} for 2 h to produce 2%X–10%MoC_{1-x}/Al_2O_3 (X: K, Na, Ce or Co). The catalyst bed was subsequently cooled down to reaction temperature in 50 ml min^{-1} N_2 flow.

FTS runs were carried out in situ in the same fixed-bed reactor by switching from the N_2 gas to syngas mixture with different H_2:CO ratios of 1:5 to 5:1 at 463–503 K and atmospheric pressure. Gas hourly space velocity (GHSV) was kept constant at 10^4 ml g_{cat}^{-1} h^{-1} with mean particle size of 100 μm for all runs. Preliminary calculations [8] indicated that there were negligible internal and external transport resistances under the reaction conditions as seen in Table 1.

BET surface area and average pore volume were measured on Quantachrome Autosorb-1 unit using nitrogen physisorption

* Corresponding author. Tel.: +61 2 9385 5268; fax: +61 2 9385 5966.
E-mail address: a.adesina@unsw.edu.au (A.A. Adesina).

0920-5861/$ – see front matter © 2011 Elsevier B.V. All rights reserved.
doi:10.1016/j.cattod.2011.04.045

Table 1
Preliminary calculations for ensuring negligible transport resistances.

External mass transport resistance	
$\frac{r_{exp} d_p r'(C_g)}{0.3 k_c r(C_g)} = 2 \times 10^{-5} << 1$	r_{exp}: CO consumption rate (mol g_{cat}^{-1} s^{-1}) d_p: catalyst particle diameter C_g: gas phase concentration of reactant $r(C_g)$: reaction rate at C_g $r'(C_g)$: the first derivative of CO reaction rate evaluated at C_g k_c: mass transfer coefficient between catalyst particle and fluid phase
External heat transfer resistance	
$\left\lvert \frac{(-\Delta H_{rxn}) d_p r_{exp} Ea}{0.3 h R_g T_g^2} \right\rvert = 1.54 \times 10^{-3} << 1$	$-\Delta H_{rxn}$: heat of reaction h: fluid-particle heat transfer coefficient T_g: bulk gas phase temperature (K)
Intraparticle mass transport resistance	
$\frac{r_{exp} d_p^2 r'(C_g)}{3 D_{eff} r(C_g)} = 1.80 \times 10^{-5} << 1$	D_{eff}: effective diffusivity of reactant
Intraparticle heat transfer resistance	
$\left\lvert \frac{(-\Delta H_{rxn}) d_p^2 r_{exp} Ea}{3 \lambda_{eff} R_g T_s^2} \right\rvert = 2.29 \times 10^{-5} << 1$	λ_{eff}: thermal conductivity of catalyst particles T_s: surface temperature E_a: activation energy R_g: universal gas constant

at 77 K. Temperature-programmed carburization between alumina-supported MoO_3 with $H_2/C_3H_8 = 5{:}1$ was performed in a ThermoCahn TGA 2121 unit from 303 to 973 K with different ramping rates. Temperature-programmed desorption runs including NH_3-TPD, CO_2-TPD, H_2-TPD and CO-TPD were carried out on a Micromeritics 2910 AutoChem to quantify the heat of desorption and site concentration for acid and basic centres as well as H_2 and CO adsorption sites respectively. The catalyst sample was exposed to 10%NH_3, 10%CO_2, 10%H_2 and 10%CO diluted in inert gas, respectively at 423 K for 1 h followed by controlled heating to 973 K with 5 different heating rates of 5, 10, 15, 20 and 30 K min^{-1}. X-ray diffraction measurements of synthesized alumina-supported Mo carbide catalysts were carried out in a Philips X'pert Pro MPD system using Ni-filtered Cu Kα (λ = 1.542 Å) operating at 45 kV and 40 mA.

3. Results and discussion

3.1. X-ray diffraction measurements

The XRD patterns of the MoC_{1-x}/Al_2O_3 catalysts are shown in Fig. 1. The Joint Committee on Powder Diffraction Standards (JCPDS) database [9] was used to analyze XRD experimental data in all cases. As seen in all diffractograms, γ-Al_2O_3 phase was detected with high intensity peaks located at $2\theta = 45.7^\circ$ and 66.7°. The peaks observed at $2\theta = 36.6^\circ$ and 61.3° for both unpromoted and promoted Mo carbide catalysts were ascribed to the formation of [1 1 1] and [2 2 0] face-centred cubic (FCC) α-MoC_{1-x}, respectively while hexagonal closed packed (HCP) β-MoC_{1-x} ($2\theta = 34.0^\circ$ and 39.5°) was also formed during carburization. The identical peaks belonging to MoO_3 (located at $2\theta = 23.40^\circ$, 25.50° and 26.75°) were not detectable in any solid suggesting that the MoO_3 precursor was converted completely to MoC_{1-x}.

The XRD pattern of 2%Ce–10%MoC_{1-x}/Al_2O_3 (b) (cf. Fig. 1b) also have peaks at 28.53° and 56.40° which were assigned to [1 1 1] and [3 1 1] CeO_2 which was produced during calcination in air, via;

$$4Ce(NO_3)_3 + O_2 \rightarrow 4CeO_2 + 6N_2O_5\uparrow \quad (1)$$

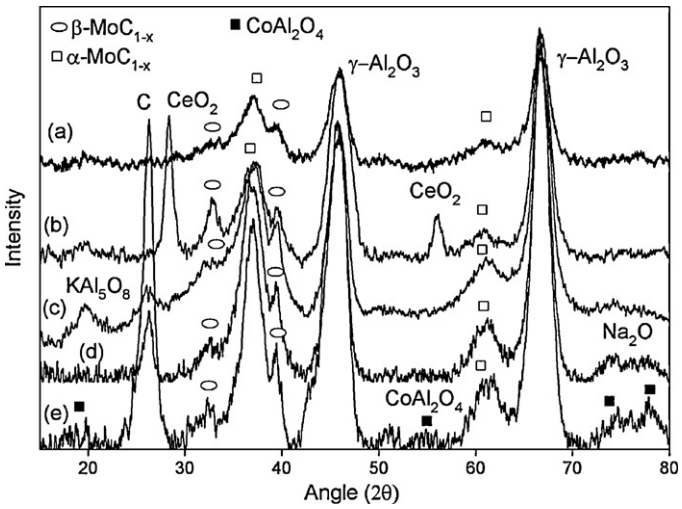

Fig. 1. XRD patterns of (a) 10%MoC_{1-x}/Al_2O_3, (b) 2%Ce–10%MoC_{1-x}/Al_2O_3, (c) 2%K–10%MoC_{1-x}/Al_2O_3, (d) 2%Na–10%MoC_{1-x}/Al_2O_3, (e) 2%Co–10%MoC_{1-x}/Al_2O_3 catalyst. (a) Temperature-programmed carburization of 2%Ce–10%MoC_{1-x}/Al_2O_3 catalyst. (b) Influence of promoter on carbide formation rate. (c) Effect of promoters on the formation of carbide phase during temperature-programmed carburization.

KAl_5O_8 phase found in K-promoted catalyst (Fig. 1, profile (c)) may be formed from;

$$K_2CO_3 \rightarrow K_2O + CO_2\uparrow \quad (2)$$

and

$$K_2O + 5Al_2O_3 \rightarrow 2KAl_5O_8 \quad (3)$$

Similarly, the production of Na_2O observed in the XRD pattern for 2%Na–10%MoC_{1-x}/Al_2O_3 catalyst arose from the decomposition reaction;

$$Na_2CO_3 \rightarrow Na_2O + CO_2\uparrow \quad (4)$$

while for Co-promoted catalyst, $CoAl_2O_4$ phase identified may be given by Eqs. (5) and (6);

$$Co(NO_3)_2 \rightarrow CoO + N_2O_5\uparrow \quad (5)$$

$$CoO + Al_2O_3 \rightarrow CoAl_2O_4 \quad (6)$$

The average size of Mo carbide particles was estimated from the Scherrer equation [10];

$$d_p = \frac{0.9\lambda}{B\cos\theta} \quad (7)$$

with d_p being particle diameter. λ and B are wavelength and peak width, respectively while θ is Bragg angle. As seen in Table 2, MoC_{1-x} particles were finely dispersed on γ-Al_2O_3 support in view of the small crystallite size ($d_p < 10$ nm) in all cases although somewhat reduced in the doped catalysts. It is also evident that the catalysts possessed high BET surface areas (177–210 m^2 g^{-1}) with pore size in the range 10–15 nm and generally larger than the size of the MoC_{1-x} particles. This further confirmed that the latter were well dispersed (cf. column 4 in Table 2). It would seem that thermal treatment during Mo oxide calcination and carburization also led to the generation of new fine pores.

3.2. Thermogravimetric study

Temperature-programmed carburization between MoO_3 with a mixture of $5H_2{:}1C_3H_8$ is shown in Fig. 2a. Each thermal profile has 2 characteristic peaks (P1 and P2) located at different temperatures suggesting that the conversion of the Mo oxide to the carbide

Table 2
Physical properties of Mo carbide catalysts.

Catalysts	Average BET surface area ($m^2\ g^{-1}$)	Average pore volume ($cm^3\ g^{-1}$)	Average pore diameter (nm)	Average crystallite size (nm)
Pure Al_2O_3	179.3	0.68	15.2	–
10%MoO_3/Al_2O_3	182.4	0.55	12.0	–
10%MoC_{1-x}/Al_2O_3	194.0	0.73	15.0	9.80
2%K–10%MoC_{1-x}/Al_2O_3	184.3	0.64	13.8	5.84
2%Na–10%MoC_{1-x}/Al_2O_3	177.40	0.60	13.5	7.37
2%Ce–10%MoC_{1-x}/Al_2O_3	210.40	0.55	10.5	6.67
2%Co–10%MoC_{1-x}/Al_2O_3	207.10	0.55	10.6	6.66

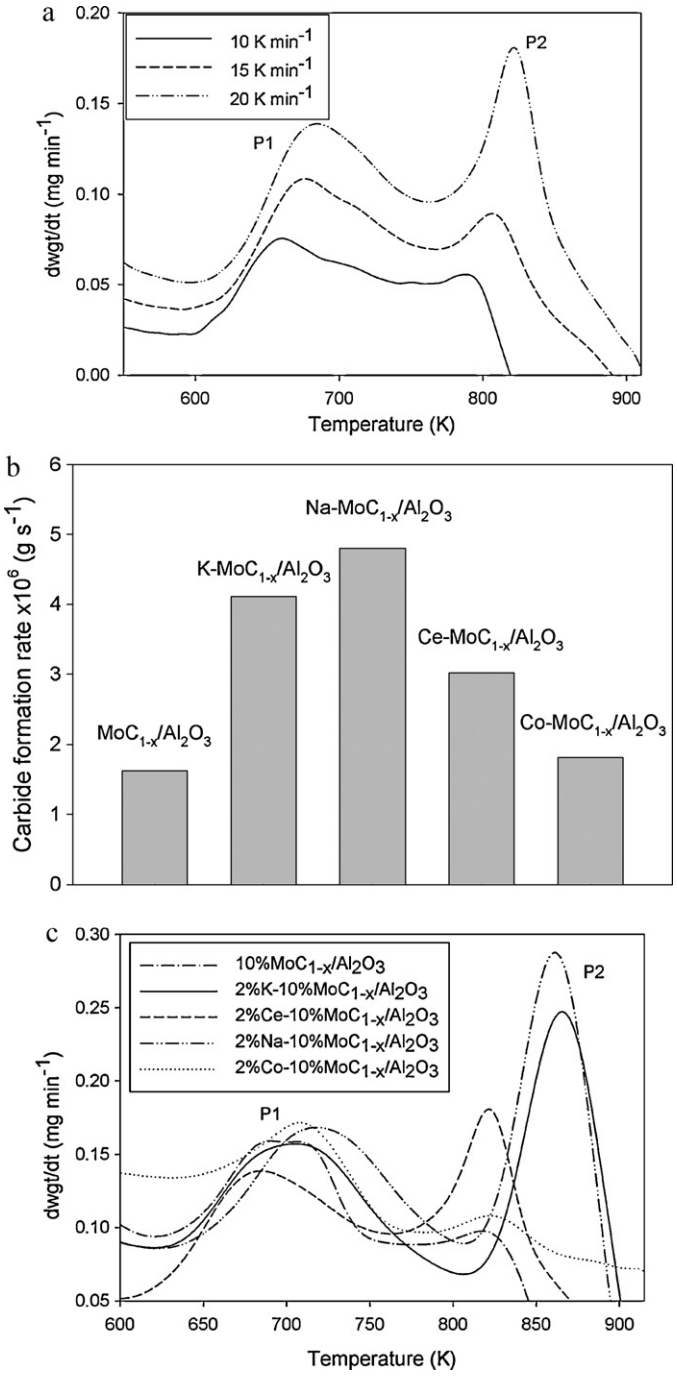

Fig. 2. Temperature-programmed carburization of unpromoted and promoted MoC_{1-x}/Al_2O_3 catalysts.

phase was a two-step process involving the formation of oxycarbide intermediate phase (P1 at 660–680 K) and the final carbide phase, P2 (790–820 K).

The effect of dopant addition on temperature-programmed carburization of MoO_3 is shown in Fig. 2b. Generally, carbide formation rate estimated from derivative weight value increased with promoter addition in the order; Na > K > Ce > Co > unpromoted Mo carbide catalysts. However, carburization temperature for the formation of carbide phase seemed to be higher for promoted catalysts, particularly K and Na-promoted MoC_{1-x} catalysts (cf. Fig. 2c).

Since the peak temperature for both P1 and P2 appeared to increase linearly with increasing heating rate as seen in Fig. 2a, the activation energy, E_a and associated pre-exponential factor, A for the production of oxycarbide and carbide phases for all MoC_{1-x} catalysts may be estimated from Kissinger equation [11];

$$\ln\left(\frac{\beta}{T_P^2}\right) = \ln\left(\frac{AR}{E_a}\right) - \frac{E_a}{RT_P} \tag{8}$$

with β, T_P, and R being heating rate, peak temperature and universal gas constant respectively.

As seen in Table 3, in general, activation energy for oxycarbide phase was lower than that of carbide form. Promoted MoC_{1-x}/Al_2O_3 catalysts possessed higher activation energy for oxycarbide production than unpromoted catalyst. Interestingly, the Arrhenius parameters for both oxycarbide and carbide phases may be related to Eq. (9) with correlation coefficient of essentially unity (0.998) as seen in Fig. 3.

$$\ln\ A_j = \sigma E_j + \theta \tag{9}$$

where σ and θ are model parameters estimated as 1.66×10^{-4}, -9.5×10^{-2} and 1.42×10^{-4}; -1.17×10^{-1} for oxycarbide and car-

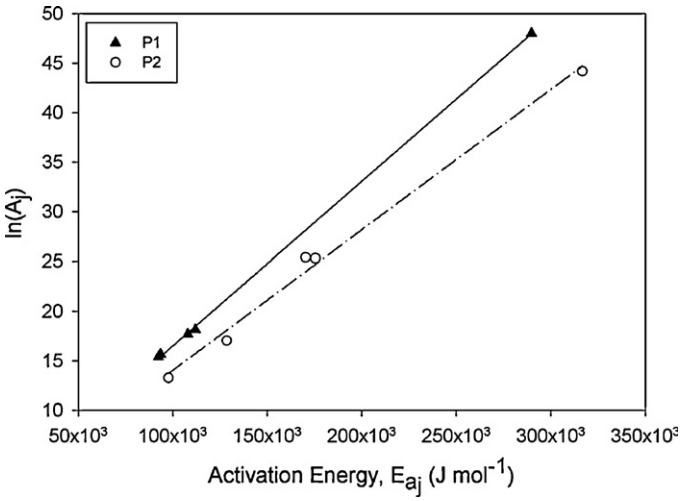

Fig. 3. Proof for the occurrence of a compensation effect for both oxycarbide and carbide phases of Mo carbide catalysts.

Table 3
Estimated activation energy, E_a and pre-exponential factor, A values for the formation of both oxycarbide and carbide phases.

Catalysts	Peak 1 (P1)		Peak 2 (P2)	
	E_a (kJ mol^{-1})	A (s^{-1})	E_a (kJ mol^{-1})	A (s^{-1})
10%MoC_{1-x}/Al_2O_3	92.40	4.75×10^6	170.30	1.09×10^{11}
2%K–10%MoC_{1-x}/Al_2O_3	112.00	7.63×10^7	128.60	2.49×10^7
2%Na–10%MoC_{1-x}/Al_2O_3	289.80	7.03×10^{20}	316.80	1.53×10^{19}
2%Ce–10%MoC_{1-x}/Al_2O_3	93.50	6.39×10^6	97.70	5.78×10^5
2%Co–10%MoC_{1-x}/Al_2O_3	108.01	4.85×10^7	175.51	9.92×10^{10}

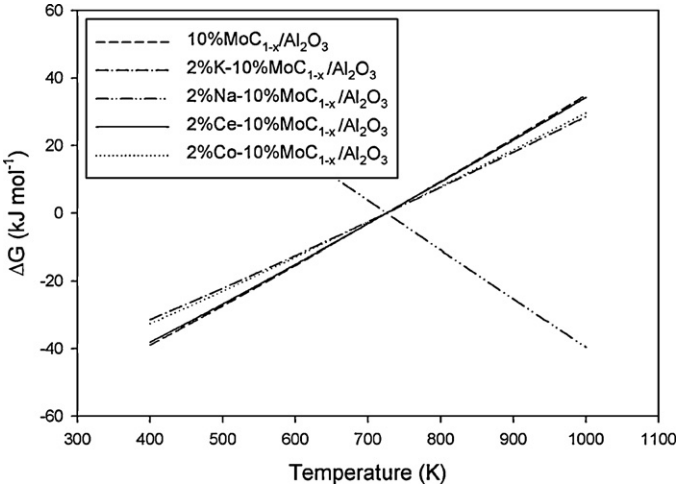

Fig. 4. Evidence for the existence of isokinetic relationship for oxycarbide phase.

bide phases, respectively. This observation implicates the presence of a 'compensation effect' for both oxycarbide and carbide phases. Indeed, the experimental data were also fitted to Eq. (10) derived from the criteria recommended by Liu and Guo [12] for the occurrence of an isokinetic relationship.

$$\Delta G_j^{\neq} = \left(\frac{1}{\sigma} - RT\right) \ln\left(\frac{A_j h}{k_B T}\right) + \theta \quad (10)$$

where h and k_B are Planck and Boltzmann constant, respectively while $\Delta G_j^{\neq}$ is the Gibbs free energy for the associated transition state complex during carburization. The unambiguous inference of an isokinetic phenomenon is guaranteed if the plots of $\Delta G_j^{\neq}$ versus T for the temperature-programmed carburization of both oxide-containing and unpromoted catalysts possess a common intersection point. Compensation effect and isokinetic phenomenon have been utilized to justify the similarity in reaction mechanism for either a particular reaction over a group of catalysts [13,14] or a series of reactions over a specific catalyst [12]. It is evident that the presence of isokinetic relationship is observed for both oxycarbide and carbide phases (cf. Figs. 4 and 5) with the corresponding isokinetic temperature, T_{iso} of 725 K and 850 K. The existence of compensation effect and isokinetic relationship for both oxycarbide and carbide phases suggests that the production of oxycarbide species from alumina-supported MoO_3 precursor and the subsequent conversion of oxycarbide to carbide phase were governed by the same topotactic mechanism in which oxygen atoms in the MoO_3 lattice were substituted by carbon atoms with negligible structural disruption regardless of the promoter type.

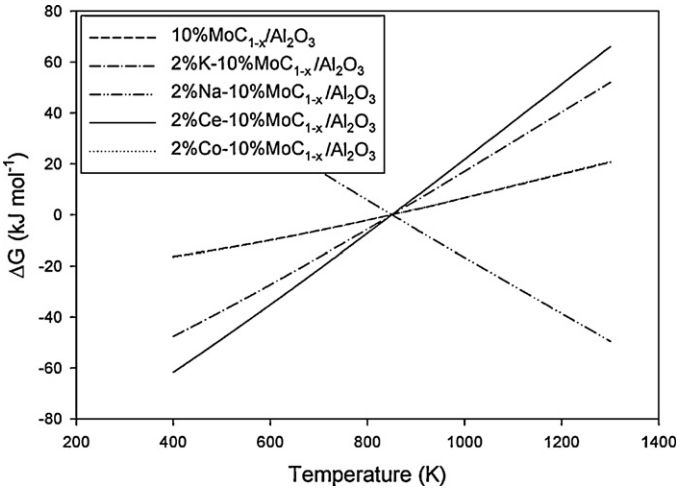

Fig. 5. Proof for the existence of isokinetic phenomenon for Mo carbide phase.

3.3. Physicochemical properties of synthesized Mo carbide catalysts

Fig. 6a shows the NH_3-TPD spectrum of MoC_{1-x} catalyst. Two discrete peaks located at different temperatures were assigned to

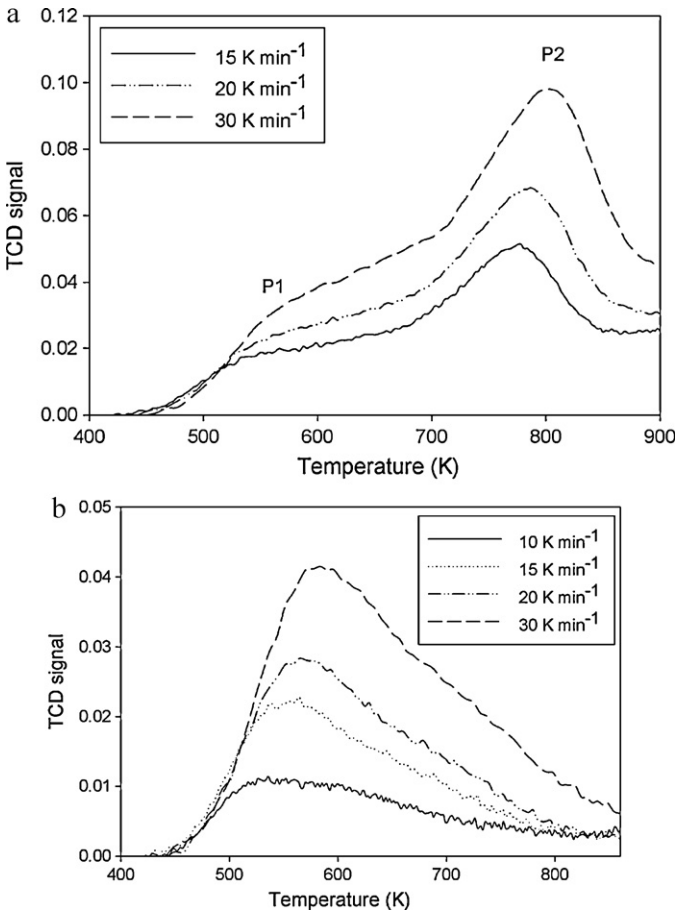

Fig. 6. NH_3-TPD of (a) 2%Co–10%MoC_{1-x}/Al_2O_3 catalyst and (b) pure Al_2O_3 support.

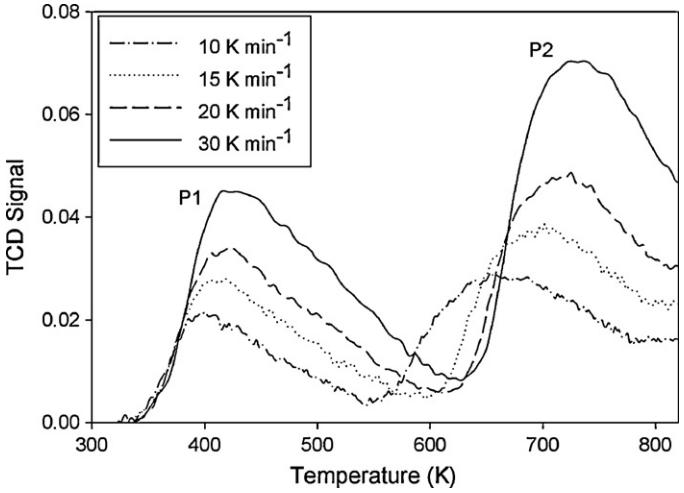

Fig. 7. CO_2-TPD of 2%Co–10%MoC_{1-x}/Al_2O_3 catalyst.

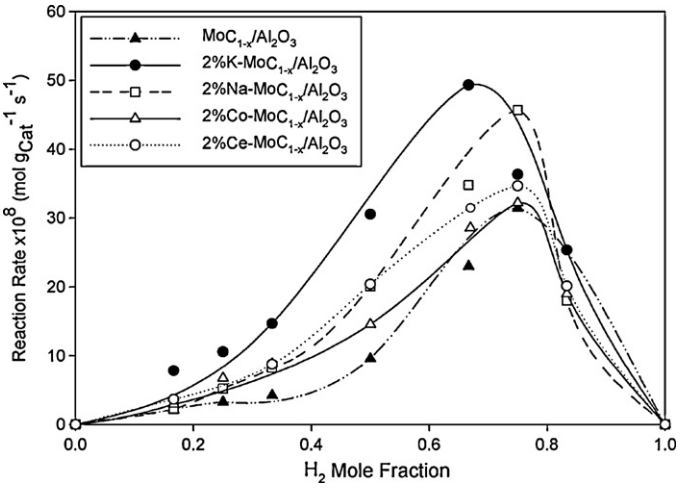

Fig. 8. Influence of feed composition on CO reaction rate of Mo carbide catalysts at 473 K.

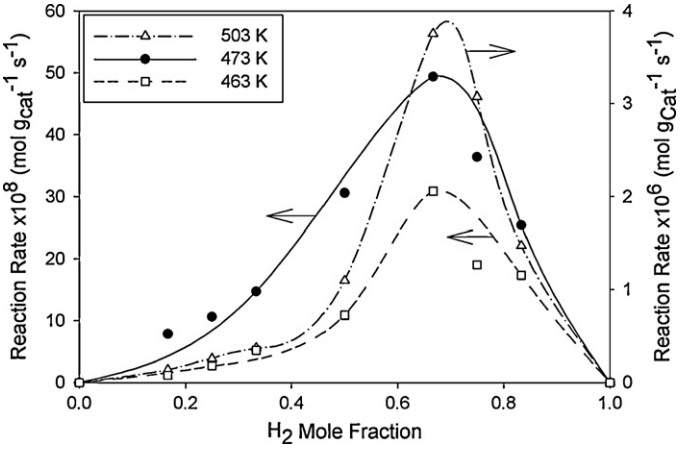

Fig. 9. Effect of reaction temperature on CO consumption rate over 2%K–10%MoC_{1-x}/Al_2O_3 catalyst.

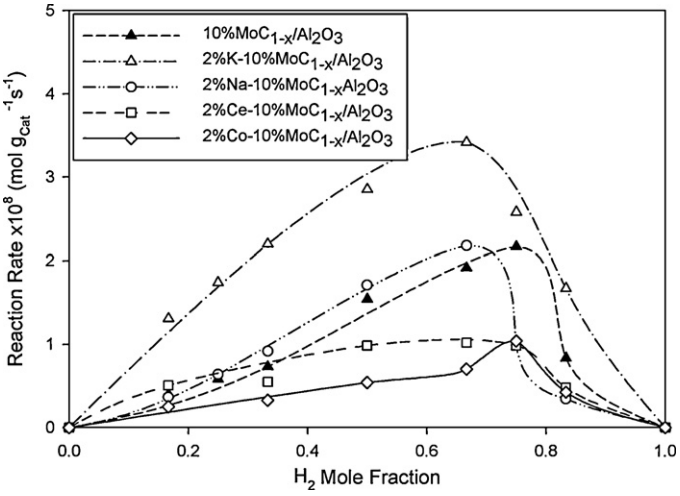

Fig. 10. Influence of promoter on olefin reaction rate over Mo carbide catalyst at 473 K.

the weak (P1) and strong (P2) acid centres. Since the weak acid site was also detected on pure calcined Al_2O_3 support (cf. Fig. 6b), it seems that the strong acid centre belongs to Mo carbide phase. Both weak (P1) and strong (P2) basic sites were also detected on catalyst surface as seen in Fig. 7.

The heat of desorption, E_d and site concentration of both acid and basic centres for Mo carbide catalysts are summarized in Table 4. Metal oxide addition reduced both NH_3 uptake and heat of desorption for strong acid site (P2) in the order; unpromoted > Co-doped > Ce-doped > Na-doped > K-doped. Not surprisingly, the strong basic site concentration was enhanced with dopant addition in the same order; K > Na > Ce > Co > unpromoted.

Although pure calcined Al_2O_3 also possessed strong basic site, the associated CO_2 heat of desorption for unpromoted and promoted MoC_{1-x} catalysts was improved due to the formation of

Table 4
Physicochemcal properties of Mo carbide catalysts.

Catalyst	MoC_{1-x}/Al_2O_3	K–MoC_{1-x}/Al_2O_3	Na–MoC_{1-x}/Al_2O_3	Co–MoC_{1-x}/Al_2O_3	Ce–MoC_{1-x}/Al_2O_3	Pure Al_2O_3 support
Adsorbed NH_3, A_{NH_3} (mol NH_3 $g_{cat}^{-1} \times 10^5$)						
P1	12.9	7.56	4.96	14.9	9.82	18.8
P2	22.2	6.39	6.58	18.6	9.59	–
Heat of desorption for NH_3 (kJ mol^{-1})						
P1	37.91	39.92	58.66	51.24	37.47	50.00
P2	320.12	60.04	97.04	119.34	118.69	–
Adsorbed CO_2, A_{CO_2} (mol CO_2 $g_{cat}^{-1} \times 10^5$)						
P1	2.72	0.43	1.20	1.40	0.19	2.64
P2	0.62	4.27	4.19	2.89	3.98	1.63
Heat of desorption for CO_2 (kJ mol^{-1})						
P1	34.91	56.96	42.18	51.48	44.04	50.00
P2	137.07	150.24	66.34	80.77	92.62	57.42
Acidic:basic site ratio						
P1	4.74	17.58	4.13	10.64	51.68	–
P2	35.81	1.50	1.57	6.44	2.41	–

Table 5
Chemisorption properties of Mo carbide catalysts.

Catalyst	MoC_{1-x}/Al_2O_3	$K–MoC_{1-x}/Al_2O_3$	$Na–MoC_{1-x}/Al_2O_3$	$Co–MoC_{1-x}/Al_2O_3$	$Ce–MoC_{1-x}/Al_2O_3$
H_2 uptake (mol H_2 $g_{cat}^{-1} \times 10^5$), Ω_{H_2}	2.31	1.45	1.53	2.35	1.07
H_2 heat of desorption (kJ mol^{-1})	63.45	34.00	33.51	31.16	21.96
CO uptake (mol CO $g_{cat}^{-1} \times 10^5$), Ω_{CO}	3.87	4.13	3.94	3.89	3.92
CO heat of desorption (kJ mol^{-1})	133.47	115.10	104.32	158.65	152.50

Table 6
Estimated activation energy for CO reaction over Mo carbide catalysts.

Catalyst	$10\%MoC_{1-x}/Al_2O_3$	$2\%K–10\%MoC_{1-x}/Al_2O_3$	$2\%Na–10\%MoC_{1-x}/Al_2O_3$	$2\%Co–10\%MoC_{1-x}/Al_2O_3$	$2\%Ce–10\%MoC_{1-x}/Al_2O_3$
E (kJ mol^{-1})	127.52	99.29	50.61	60.66	166.27
A (mol g_{cat}^{-1} s^{-1})	4.62×10^6	6.33×10^4	1.29×10^{-2}	1.05	1.47×10^{12}

Table 7
Fischer–Tropsch activity over Mo carbide catalysts at 473 K and $H_2/CO = 2:1$.

Catalyst	MoC_{1-x}/Al_2O_3	$K–MoC_{1-x}/Al_2O_3$	$Na–MoC_{1-x}/Al_2O_3$	$Co–MoC_{1-x}/Al_2O_3$	$Ce–MoC_{1-x}/Al_2O_3$
CO conversion (%)	4.76	8.54	6.02	4.95	5.45
Product selectivity (%)					
CH_4	69.52	67.14	55.36	63.38	62.97
Olefin	18.55	11.81	12.61	6.06	4.54
Paraffin	79.19	83.26	80.75	89.11	90.43
C_{5+}	2.35	3.48	7.06	4.28	5.10

carbide phase with the K-catalyst possessing the highest value. Heat of desorption for both strong basic and acid sites was superior to that of corresponding weak basic and acid centres. However, the ratio of acid to basic site concentration for both P1 and P2 is higher than unity indicating that the MoC_{1-x} catalyst surface is primarily acidic. Indeed, the acid to basic site concentration ratio for P2 followed the same trend for strong acid site concentration.

CO-TPD and H_2-TPD were also carried out to determine the strength and concentration of potential FT sites (CO and H_2 adsorption sites). As seen in Table 5, both H_2 and CO chemisorbed on MoC_{1-x} catalyst surface. Nonetheless, CO adsorption appeared to be stronger than H_2 since it had superior heat of desorption and higher uptake. This observation is in agreement with other studies [15]. In particular, the desorption temperature for CO (585 K) was above the range for FTS (453–553 K) while that for H_2 was at the lower end of this window (460 K). This means that H_2 may exist predominantly in the gas phase while reacting with chemisorbed CO on catalyst surface during FTS. As seen in Table 5, CO uptake increased with promoter addition probably due to higher electron density (donated by dopants) which facilitated CO chemisorption [16]. In contrast, promoted catalysts possess lower H_2 heat of desorption than that of unpromoted MoC_{1-x}/Al_2O_3.

3.4. Fischer–Tropsch synthesis

The influence of H_2 mole fraction, y_{H_2} on FT synthesis rate for all catalysts is illustrated in Fig. 8. CO consumption rate was improved considerably with increasing y_{H_2} and reached a maximum at $y_{H_2} = 0.67–0.75$ for the 5Mo carbide catalysts in agreement with other studies [17]. Unlike conventional FT catalysts (e.g. Co) exhibiting optimal reaction rate at higher H_2 mole fraction [18], Mo carbide catalyst seemed to be more tolerant of CO partial pressure since the active site of MoC_{1-x} has an oxycarbide structure formed in situ by CO molecular adsorption [19,20]. Indeed, the Mo carbide catalyst possessed both face-centred cubic and hexagonal closed packed structures. Therefore, the carbon deficiency in these structures may incorporate oxygen to yield an oxycarbide phase [21]. In general, the addition of the metal oxide dopant enhanced FT activity of MoC_{1-x}/Al_2O_3 catalyst, especially with K_2O and Na_2O. CO consumption rate decreased in the

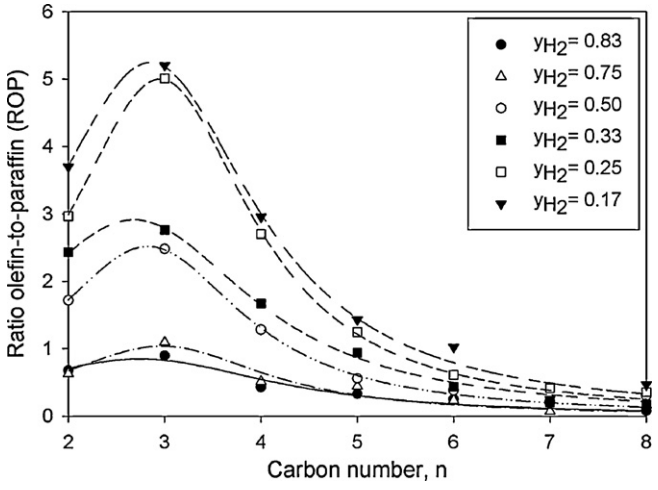

Fig. 11. Effect of H_2 mole fraction on olefin-to-paraffin ratio for $2\%K–10\%MoC_{1-x}/Al_2O_3$ catalyst at 473 K.

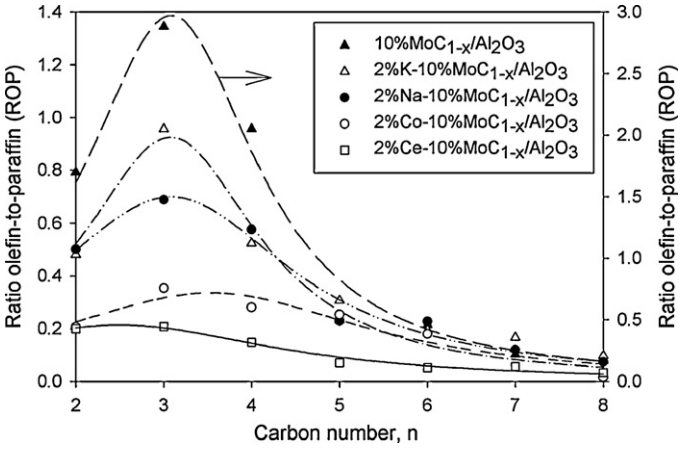

Fig. 12. Effect of promoters on olefin-to-paraffin ratio over Mo carbide catalysts at 473 K and H_2:CO = 2:1.

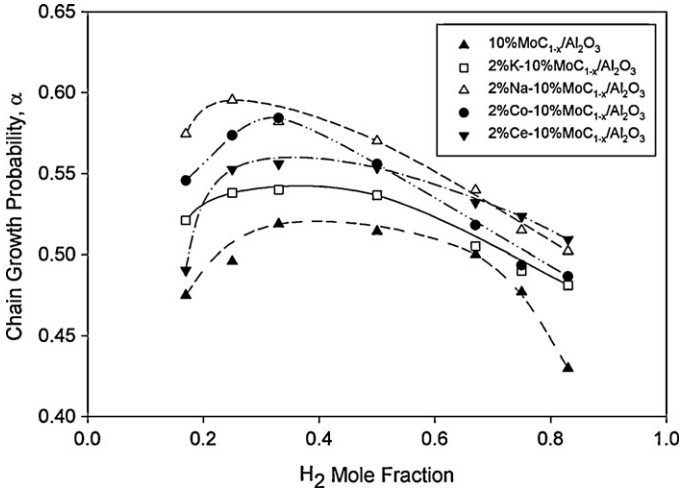

Fig. 13. Influence of feed composition on chain growth factor for Mo carbide catalysts.

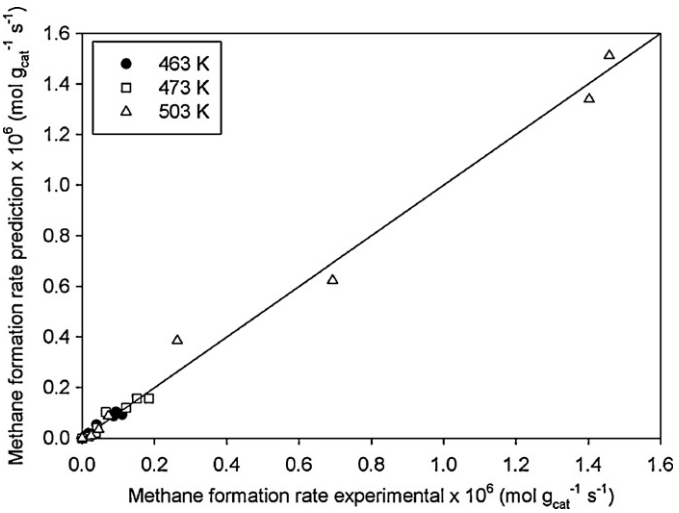

Fig. 15. Parity plot for methanation model over 2%K–10%MoC_{1-x}/Al_2O_3 catalyst.

order; K–MoC_{1-x}/Al_2O_3 > Na–MoC_{1-x}/Al_2O_3 > Ce–MoC_{1-x}/Al_2O_3 > Co–MoC_{1-x}/Al_2O_3 > MoC_{1-x}/Al_2O_3 parallel to the trend for strong basic site concentration. Interestingly, CO uptake also reduced in the same order; K > Na > Ce > Co > unpromoted catalyst (cf. Table 5) suggesting that CO adsorption site is the active site for FTS over Mo carbide catalysts.

The effect of reaction temperature on hydrocarbon production rate over 2%K–10%MoC_{1-x}/Al_2O_3 catalyst is shown in Fig. 9. Optimal rate observed at $y_{H_2} = 0.67$ was unchanged with reaction temperature. Activation energy for the CO consumption rate over Mo carbide catalysts is summarized in Table 6.

Additionally, compensation effect and isokinetic phenomenon were also implicated for the FTS reaction over the Mo carbide catalyst system with T_{iso} of 450 K and $\sigma = 2.67 \times 10^{-4}$ mol J^{-1}; $\theta = -16.93$.

Fischer–Tropsch activity and selectivity over promoted Mo carbide catalysts at 473 K and $H_2/CO = 2:1$ are summarized in Table 7. CO conversion was improved with promoted MoC_{1-x} catalysts while methane selectivity reduced with promoter addition from 69.5 to 55.4%. Additionally, doped Mo carbide catalysts enhanced higher hydrocarbons, C_{5+} selectivity. Na promoter seemed to be the optimal dopant for Mo carbide catalyst in terms of CH_4 suppression and C_{5+} selectivity while K-promoted catalyst possessed highest CO conversion. However, olefin selectivity decreased with dopant addition in the order; unpromoted catalyst > Na-doped > K-doped > Co-doped > Ce-doped catalyst.

As seen in Fig. 10, olefin synthesis rate over MoC_{1-x} catalyst improved with alkaline promoter (K and Na) and had an optimum at the same hydrogen mole fraction for highest CO consumption rate ($y_{H_2} = 0.67$) while a reduction in olefin formation rate (below that for unpromoted MoC_{1-x}) was observed with Co and Ce dopants. Interestingly, these 2 promoters have higher CO heat of desorption than the unpromoted catalyst while both K and Na possess low values (cf. Table 5).

As seen in Figs. 11 and 12, olefin-to-paraffin ratio (*ROP*) is a function of carbon number and attained an optimum at C_3 for all feed compositions. However, *ROP* reduced exponentially with growing chain length beyond C_3 due to increasing adsorptivity or lower diffusion coefficients for α-olefins [22,23]. The anomalous *ROP* for C_2 (lower than *ROP* of C_3) was ascribed to the readsorption of ethene for secondary reactions, namely; hydrogenation to ethane and incorporation of ethene for chain growth propagation [24]. Additionally, olefin-to-paraffin ratio diminished with increased H_2 mole fraction (cf. Fig. 11) in agreement with both previous experimental studies with cobalt catalyst [25] and theoretical models derived from common FT mechanisms [26,27].

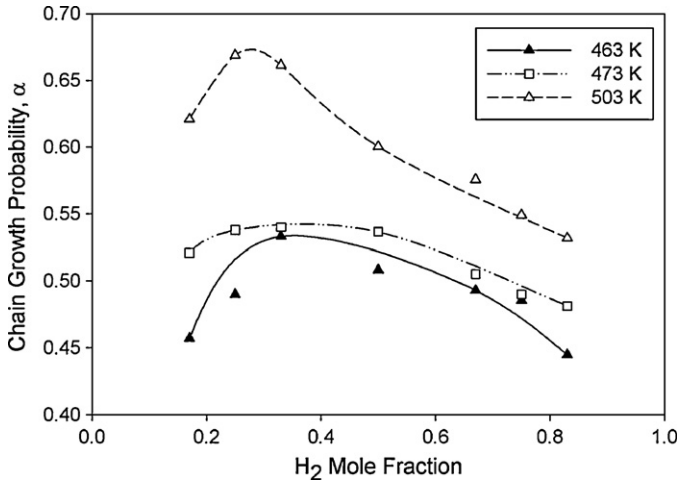

Fig. 14. Effect of reaction temperature and feed composition on chain growth probability of 2%K–10%MoC_{1-x}/Al_2O_3 catalyst.

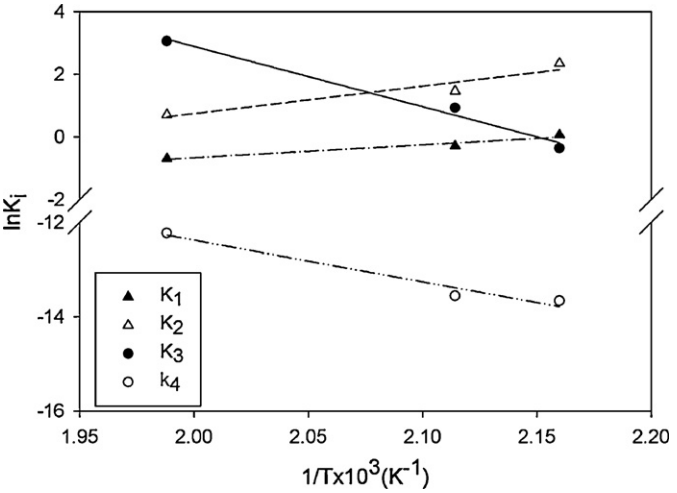

Fig. 16. Estimated activation energy for formation of CH_4 and HCOH species over 2%K–10%MoC_{1-x} catalysts.

Table 8
Methanation reaction models.

Model no.	Mechanism	Model
I	$MoC_{1-x} + CO \underset{k_{-1}}{\overset{k_1}{\rightleftarrows}} X$ $2X + H_2 \underset{k_{-2}}{\overset{k_2}{\rightleftarrows}} 2H_X$ $CO + X \underset{k_{-3}}{\overset{k_3}{\rightleftarrows}} CO_X$ $CO_X + 2H_X \xrightarrow{k_4} CH_{2X} + O_X + X$ $CH_{2X} + 2H_X \rightarrow CH_4 + 3X$ $2H_X + O_X \rightarrow H_2O + 3X$	$r_{C_1} = \frac{k_{1234} P_{CO}^4 P_{H_2}}{(1+K_1 P_{CO} + K_{12} P_{H_2}^{1/2} P_{CO} + K_{13} P_{CO}^2)^3}$ where $K_{12} = K_1 K_2^{1/2}$, $K_{13} = K_1 K_3$ and $k_{1234} = k_4 K_2 K_3 K_1^3$
II	$MoC_{1-x} + CO \underset{k_{-1}}{\overset{k_1}{\rightleftarrows}} X$ $CO + X \underset{k_{-2}}{\overset{k_2}{\rightleftarrows}} CO_X$ $CO_X + H_2 \underset{k_{-3}}{\overset{k_3}{\rightleftarrows}} HCOH_X$ $HCOH_X + 2H_2 \xrightarrow{k_4} CH_4 + H_2O + X$	$r_{C_1} = \frac{k_{1234} P_{H_2}^3 P_{CO}^2}{(1+K_1 P_{CO} + K_{12} P_{CO}^2 + K_{123} P_{CO}^2 P_{H_2})}$ where $K_{12} = K_1 K_2$, $K_{123} = K_1 K_2 K_3$ and $k_{1234} = k_4 K_{123}$.
III	$MoC_{1-x} + CO \underset{k_{-1}}{\overset{k_1}{\rightleftarrows}} X$ $X + H_2 \underset{k_{-2}}{\overset{k_2}{\rightleftarrows}} H_{2X}$ $CO + X \underset{k_{-3}}{\overset{k_3}{\rightleftarrows}} CO_X$ $CO_X + H_{2X} \xrightarrow{k_4} CH_{2X} + O_X$ $CH_{2X} + H_{2X} \rightarrow CH_4 + 2X$ $H_{2X} + O_X \rightarrow H_2O + 2X$	$r_{C_1} = \frac{k_{1234} P_{CO}^3 P_{H_2}}{(1+K_1 P_{CO} + K_{12} P_{H_2} P_{CO} + K_{13} P_{CO}^2)^2}$ where $K_{12} = K_1 K_2$, $K_{13} = K_1 K_3$ and $k_{1234} = k_4 K_2 K_3 K_1^2$
IV	$MoC_{1-x} + CO \underset{k_{-1}}{\overset{k_1}{\rightleftarrows}} X$ $CO + X \underset{k_{-2}}{\overset{k_2}{\rightleftarrows}} CO_X$ $CO_X + 2H_2(g) \xrightarrow{k_3} CH_{2X} + H_2O \uparrow$ $CH_{2X} + H_2(g) \rightarrow CH_4 + X$	$r_{C_1} = \frac{k_{123} P_{CO}^2 P_{H_2}^2}{1+K_1 P_{CO} + K_{12} P_{CO}^2}$ where $K_{12} = K_1 K_2$ and $k_{123} = k_3 K_1 K_2$

Product distribution in FTS is typically governed by a polymerization scheme and the hydrocarbon formation rates may be captured by the Anderson–Schulz–Flory (ASF) model [28] given by;

$$r_n = k_{ASF}(1-\alpha)^2 \alpha^{n-1} \quad (11)$$

where r_n is the production rate for hydrocarbons with carbon number, n. k_{ASF} is the Anderson–Schulz–Flory constant while α is the chain growth probability. Fig. 13 shows the influence of H_2 mole fraction on chain growth factor. All catalysts exhibited highest α value at $y_{H_2} = 0.25 - 0.33$. However, beyond 0.33, chain growth probability reduced with increasing H_2 mole fraction in agreement with similar studies on traditional FT catalysts [29]. Reaction temperature seemed to improve chain growth probability regardless of feed composition (cf. Fig. 14). However, the chain growth factor may decrease at some reaction temperature (in spite of the higher propagation rate) due to increasing termination rate of olefinic species on catalyst surface to paraffins and

Table 9
Model parameter estimates at different reaction temperatures.

Model no.	Temperature (K)	K_1	K_2	K_3	k_4	k_3	R^2
I	463	10.57	1.06	1.78	2.46×10^{-7}	–	0.96
	473	4.28	0.63	4.86	4.39×10^{-6}	–	0.95
	503	5.94	3.37	1.67	1.85×10^{-7}	–	0.99
II	463	1.06	10.45	0.70	1.17×10^{-6}	–	0.98
	473	0.75	4.31	2.51	1.30×10^{-6}	–	0.97
	503	0.50	2.03	21.17	4.87×10^{-6}	–	0.97
III	463	−1.22	2.82	−17.41	-2.42×10^{-7}	–	0.95
	473	0.16	−26.34	102.09	-3.44×10^{-7}	–	0.95
	503	−2.57	1.48	−4.83	-4.91×10^{-7}	–	0.98
IV	463	−5.60	−3.81	–	–	1.33×10^{-7}	0.96
	473	−4.99	−3.24	–	–	2.28×10^{-7}	0.95
	503	−6.81	−2.07	–	–	5.53×10^{-7}	0.98

Table 10
Estimated model parameters for methanation reaction (model II) over 2%K–MoC_{1-x}/Al_2O_3.

Model parameters	463 K	473 K	503 K	
K_1 (atm^{-1})	1.06	0.75	0.50	BMV criteria
K_2 (atm^{-1})	10.45	4.31	2.03	
K_3 (atm^{-1})	0.70	2.51	21.17	
k_4 ($\times 10^6$ mol g_{cat}^{-1} s^{-1} atm^{-2})	1.17	1.30	4.87	
ΔH_1 (cal mol^{-1})		−8168.24		Satisfied
ΔS_1 (cal mol^{-1} K^{-1})		−17.66		
ΔH_2 (cal mol^{-1})		−17411.60		Satisfied
ΔS_2 (cal mol^{-1} K^{-1})		−33.35		
E_{CH_4} (kJ mol^{-1})		73.1		
E_{HCOH} (kJ mol^{-1})		160.0		

decreasing re-adsorptivity of α-olefins for chain growth propagation [30]. Mo carbide catalyst reportedly has lower α value (≤0.4) [31–34] than Co or Fe FT catalysts. Nevertheless, the addition of promoter may improve chain growth factor (up to 0.6) as seen in Fig. 13 and chain growth probability decreased in the order, Na > Co > Ce > K > unpromoted.

Based on the CO-TPD and H_2-TPD results earlier discussed, H_2 may exist in the gas phase while reacting with chemisorbed CO on the Mo carbide catalyst. Indeed, Clair et al. reported that CO adsorbed molecularly on MoC_{1-x} catalyst surface [35]. Therefore, the methanation reaction may be expressed by the Eley–Rideal mechanism below;

$$MoC_{1-x} + CO \underset{k_{-1}}{\overset{k_1}{\rightleftarrows}} X \quad \text{(site generation step)} \tag{12}$$

$$CO + X \underset{k_{-2}}{\overset{k_2}{\rightleftarrows}} CO_X \tag{13}$$

$$CO_X + H_2 \underset{k_{-3}}{\overset{k_3}{\rightleftarrows}} HCOH_X \tag{14}$$

$$HCOH_X + 2H_2 \xrightarrow{k_4} CH_4 + H_2O + X \tag{15}$$

From Eqs. (12)–(14), the fractional surface coverage for species i, θ_i may be obtained as;

$$\theta = K_1 P_{CO} \theta_0 \tag{16}$$

$$\theta_{CO} = K_2 P_{CO} \theta \tag{17}$$

$$\theta_{HCOH} = K_3 P_{H_2} \theta_{CO} \tag{18}$$

with $K_1 = k_1/k_{-1}$, $K_2 = k_2/k_{-2}$ and $K_3 = k_3/k_{-3}$. θ_0 is the initial fractional site vacancy on the MoC_{1-x} and θ is fractional active site formed in situ by co-ordinative bonding of CO to a vacant Mo site.

Reaction (15) between adsorbed HCOH and gas phase H_2 was considered as the irreversible rate-controlling step. Thus, methane reaction rate may be given as;

$$r_{C_1} = k_4 \theta_{HCOH} P_{H_2}^2 \tag{19}$$

If θ_{CO} and θ_{HCOH} are assumed as the most abundant surface species on Mo carbide catalyst, the site balance may be written as;

$$1 = \theta_0 + \theta + \theta_{CO} + \theta_{HCOH} \tag{20}$$

By combining Eqs. (16)–(20), methanation reaction rate may be derived as;

$$r_{C_1} = \frac{k_{1234} P_{H_2}^3 P_{CO}^2}{1 + K_1 P_{CO} + K_{12} P_{CO}^2 + K_{123} P_{CO}^2 P_{H_2}} \tag{21}$$

where $K_{12} = K_1 K_2$, $K_{123} = K_1 K_2 K_3$, and $k_{1234} = k_4 K_{123}$.

By the same token, methanation models based on both carbide and enolic mechanisms were also derived and summarized in Table 8.

Non-linear regression analysis of the experimental data was carried out to estimate the associated parameters using Polymath 6.0 software. As seen in Table 9, all proposed models exhibited a good fit to the experimental data with $R^2 > 0.95$. However, models III and IV gave negative adsorption equilibrium constants and were deemed unacceptable.

Further discrimination between models I and II was performed based on, the thermodynamic consistency of adsorption equilibrium constants (K_1 and K_2). This was subsequently assessed against the Boudart–Mears–Vannice (BMV) criteria [36] as seen in Eqs. (22) and (23).

$$0 < -\Delta S_i < \Delta S_{i_g} \tag{22}$$

$$10 \le -\Delta S_i \le 12.2 - 0.0014 \Delta H_i \tag{23}$$

with ΔS_{i_g} being entropy of CO in gas phase, 47.3 cal mol^{-1} K^{-1}. ΔH_i and ΔS_i are experimental enthalpy (cal mol^{-1}) and entropy changes (cal mol^{-1} K^{-1}), respectively, estimated from Eq. (24).

$$\ln K_i = -\frac{\Delta H_i}{RT} + \frac{\Delta S_i}{R} \tag{24}$$

It is evident that model I did not meet the thermodynamic criteria since the associated model parameters at different reaction temperatures did not Eq. (24). Even so, the values of ΔH_i and ΔS_i summarized in Table 10 for both equilibrium constants K_1 and K_2 of model II satisfied the BMV criteria. In addition, as seen in parity plot (cf. Fig. 15), the proposed methanation model II is in good agreement with experimental data. As a result, the Eley–Rideal mechanism (model II) in which gas phase H_2 reacts with molecularly chemisorbed CO on catalyst surface to form HCOH species appeared to be the most appropriate model for capturing methane formation over promoted Mo carbide catalysts. Moreover, the activation energy values for the formation of CH_4 and chain initiator HCOH species were also estimated as 73.1 and 160.0 kJ mol^{-1}, respectively with corresponding pre-exponential factor of 1.80×10^2 and 9.31×10^{17} mol g_{cat}^{-1} s^{-1} as seen in Fig. 16.

4. Conclusions

Mo carbide catalysts (unpromoted and doped samples) were prepared by temperature-programmed carburization using H_2:C_3H_8 as carburizing gas. The method yielded high surface area catalysts between 194 to 210 m^2 g^{-1} close to that of pure Al_2O_3. Temperature-programmed carburization between MoO_3/Al_2O_3 precursor and H_2/C_3H_8 was a two-step process via the formation of oxycarbide intermediate phase. The existence of a compensation effect and an isokinetic phenomenon for both oxycarbide and carbide phases indicated that the same topotactic mechanism governed the conversion of MoO_3 to oxycarbide and carbide

phases. Although H_2 and CO adsorbed on Mo carbide catalyst surface, CO chemisorption seemed to be superior to H_2 adsorption and the latter may preferentially remain unadsorbed in the presence of chemisorbing CO. There was an increase in CO uptake with doped MoC_{1-x} catalysts. Weak and strong basic centres as well as acid sites were detected on the MoC_{1-x} catalyst surface. Strong basic site concentration reduced in the order; K-MoC_{1-x}/Al_2O_3 > Na–MoC_{1-x}/Al_2O_3 > Ce–MoC_{1-x}/Al_2O_3 > Co–MoC_{1-x}/Al_2O_3 > MoC_{1-x}/Al_2O_3 which was also the trend for CO reaction rate. All catalysts attained maximum FT activity at $y_{H_2} = 0.67–0.75$ and chain growth probability was generally improved by promoter addition. Methane formation was suppressed with doped-catalysts, particularly Na-promoted MoC_{1-x} catalyst while increasing C_{5+} selectivity was observed for 4 promoted catalysts. Olefin-to-paraffin ratio reduced with increasing chain length and H_2 mole faction. Methanation reaction over Mo carbide catalysts may be captured by an Eley–Rideal kinetic model in which gas phase H_2 reacted with molecularly adsorbed CO on catalyst surface to form chain initiator, HCOH.

Acknowledgements

The authors are grateful to Australian Research Council for financial support.

References

[1] R.L. Levy, M. Boudart, Science 181 (1973) 547–549.
[2] R. Kojima, K.-i. Aika, Appl. Catal. A: Gen. 219 (2001) 141–147.
[3] Z. Yao, C. Shi, Catal. Lett. 130 (2009) 239–245.
[4] S. Li, J.S. Lee, T. Hyeon, K.S. Suslick, Appl. Catal. A: Gen. 184 (1999) 1–9.
[5] A.R.S. Darujati, W.J. Thomson, Appl. Catal. A: Gen. 296 (2005) 139–147.
[6] T. Xiao, H. Wang, J. Da, K.S. Coleman, M.L.H. Green, J. Catal. 211 (2002) 183–191.
[7] T. Xiao, A.P.E. York, K.S. Coleman, J.B. Claridge, J. Sloan, J. Charnock, M.L.H. Green, J. Mater. Chem. 11 (2001) 3094–3098.
[8] H.S. Fogler, Elements of Chemical Reaction Engineering, 4th ed., Pearson Education, United States, 2006.
[9] JCPDS Powder Diffraction File, International Centre for Diffraction Date, PA, 2000.
[10] A.L. Patterson, Phys. Rev. 56 (1939) 978.
[11] M.E. Brown, Introduction to Thermal Analysis: Techniques and Application, Kluwer Academic Publishers, The Netherlands, 2001.
[12] L. Liu, Q.X. Guo, Chem. Rev. 101 (2001) 673–696.
[13] G.C. Bond, Catal. Today 49 (1999) 41–48.
[14] J. Zhang, H. Xu, W. Li, Appl. Catal. A: Gen. 296 (2005) 257–267.
[15] J.S. Lee, K.H. Lee, J.Y. Lee, J. Phys. Chem. 96 (1992) 362–366.
[16] D.B. Bukur, D. Mukesh, S.A. Patel, Ind. Eng. Chem. Res. 29 (1990) 194–204.
[17] M. Saito, R.B. Anderson, J. Catal. 63 (1980) 438–446.
[18] A.A. Adesina, R.R. Hudgins, P.L. Silveston, Can. J. Chem. Eng. 64 (1986) 447–454.
[19] C. Phamhuu, M.J. Ledoux, J. Guille, J. Catal. 143 (1993) 249–261.
[20] J.B. Claridge, A.P.E. York, A.J. Brungs, C. Marquez-Alvarez, J. Sloan, S.C. Tsang, M.L.H. Green, J. Catal. 180 (1998) 85–100.
[21] E. Furimsky, Appl. Catal. A: Gen. 240 (2003) 1–28.
[22] D.B. Bukur, L. Nowicki, X. Lang, Catal. Today 24 (1995) 111–119.
[23] E.W. Kuipers, I.H. Vinkenburg, H. Oosterbeek, J. Catal. 152 (1995) 137–146.
[24] D.S. Jordan, A.T. Bell, J. Phys. Chem. 90 (1986) 4797–4805.
[25] C.G. Cooper, T.-H. Nguyen, Y.-J. Lee, K.M. Hardiman, T. Safinski, F.P. Lucien, A.A. Adesina, Catal. Today 131 (2008) 255–261.
[26] A.A. Adesina, J. Mol. Catal. 62 (1990) L23–L27.
[27] A.T. Bell, Catal. Rev. Sci. Eng. 23 (1981) 203–232.
[28] R.B. Anderson, The Fischer–Tropsch synthesis, Academic Press, New York, 1984.
[29] T.J. Donnelly, C.N. Satterfield, Appl. Catal. 52 (1989) 93–114.
[30] G.P. Van der Laan, A.A.C.M. Beenackers, Catal. Rev. Sci. Eng. 41 (1999) 255–318.
[31] H.C. Woo, K.Y. Park, Y.G. Kim, I.-S. Nam, J.S. Chung, J.S. Lee, Appl. Catal. 75 (1991) 267–280.
[32] K.Y. Park, W.K. Seo, J.S. Lee, Catal. Lett. 11 (1991) 349–356.
[33] M. Xiang, D. Li, H. Xiao, J. Zhang, H. Qi, W. Li, B. Zhong, Y. Sun, Fuel 87 (2008) 599–603.
[34] A. Griboval-Constant, J.-M. Giraudon, G. Leclercq, L. Leclercq, Appl. Catal. A: Gen. 260 (2004) 35–45.
[35] T.P. St. Clair, S.T. Oyama, D.F. Cox, Surf. Sci. 468 (2000) 62–76.
[36] M. Boudart, D.E. Mears, M.A. Vannice, Ind. Chim. Belge 32 (1967) 281.